

Calcium batteries: synergistic effects of Ca(BF4)2 and acetonitrile for calcium deposition/stripping

Downloaded from: https://research.chalmers.se, 2025-10-30 06:30 UTC

Citation for the original published paper (version of record):

Mihalinec, G., Bafti, A., Johansson, P. et al (2025). Calcium batteries: synergistic effects of Ca(BF4)2 and acetonitrile for calcium deposition/stripping. JPhys Energy, 7(4). http://dx.doi.org/10.1088/2515-7655/adff32

N.B. When citing this work, cite the original published paper.

research.chalmers.se offers the possibility of retrieving research publications produced at Chalmers University of Technology. It covers all kind of research output: articles, dissertations, conference papers, reports etc. since 2004. research.chalmers.se is administrated and maintained by Chalmers Library



PAPER • OPEN ACCESS

Calcium batteries: synergistic effects of ${\rm Ca(BF_4)_2}$ and acetonitrile for calcium deposition/stripping

To cite this article: Grgur Mihalinec et al 2025 J. Phys. Energy 7 045021

View the article online for updates and enhancements.

You may also like

- 2024 roadmap for sustainable batteries Magda Titirici, Patrik Johansson, Maria Crespo Ribadeneyra et al.
- Recent status and future prospects of emerging oxygen vacancy-/defect-rich electrode materials: from creation mechanisms to detection/quantification techniques, and their electrochemical performance for rechargeable batteries Sandeep Kumar Sundriyal and Yogesh Sharma
- <u>Polymerization-enhanced flexible</u> <u>perovskite solar cells: a mini review</u> Sihao Huang, Bin Han, Shuyan Chen et al.

Journal of Physics: Energy



OPEN ACCESS

RECEIVED

18 April 2025

REVISED

10 August 2025

ACCEPTED FOR PUBLICATION

26 August 2025

PUBLISHED

19 September 2025

Original content from this work may be used under the terms of the Creative Commons Attribution 4.0 licence.

Any further distribution of this work must maintain attribution to the author(s) and the title of the work, journal citation and DOI.



PAPER

Calcium batteries: synergistic effects of $Ca(BF_4)_2$ and acetonitrile for calcium deposition/stripping

Grgur Mihalinec¹, Arijeta Bafti¹, Patrik Johansson^{2,3} and Zoran Mandić^{1,*}

- $^{
 m l}$ University of Zagreb, Faculty of Chemical Engineering and Technology, Trg Marka Marulića 19, Zagreb 1000, Croatia
- ² Department of Physics, Chalmers University of Technology, SE-412 96 Goteborg, Sweden
- 3 ALISTORE-European Research Institute, FR CNRS 3104, Hub de l'Energie 15, Rue Baudelocque, 80039 Amiens, France
- * Author to whom any correspondence should be addressed.

E-mail: zmandic@fkit.unizg.hr

Keywords: calcium battery, deposition/stripping, synergistic effect, acetonitrile, corrosion, passivation Supplementary material for this article is available online

Abstract

Details of the interfacial reactions at calcium metal electrodes using three different electrolytes—Ca(BF₄)₂ or Ca(TFSI)₂ in acetonitrile (ACN), and Ca(BF₄)₂ in an ethylene carbonate: propylene carbonate (EC:PC) mixture—are here revealed using a set of electrochemical techniques: cyclic voltammetry, open-circuit potential, electrochemical impedance spectroscopy, and electrochemical quartz crystal microbalance. Furthermore, the deposition/stripping of calcium on electrodes/substrates of calcium metal and stainless steel (SS), and the products formed, are assessed by x-ray diffraction, Fourier transform infrared spectroscopy, and scanning electron microscopy. Combined, these show that calcium undergoes corrosion, resulting in the formation of pits, if polarized at sufficient positive potentials, but also that spontaneous formation of passivation layers proceeds through two or more steps at different rates in different electrolytes. The cathodic degradation of ACN is suppressed by the presence of Ca salts in the electrolyte, while the calcium deposition is strongly inhibited in both the $Ca(TFSI)_2$ in ACN and the $Ca(BF_4)_2$ in EC:PC electrolytes due to the simultaneous formation of the passivation layer. Deposition from the $Ca(BF_4)_2$ in ACN electrolyte, however, is enabled by the formation of a passivation layer that proceeds at lower rates, and stripping can proceed at an appreciable rate. On inert SS substrates/electrodes, the calcium deposition goes through two stages, the first being underpotential deposition at a potential of approximately 1 V more positive than the thermodynamic potential. Altogether, we showcase ways to truly deposit/strip calcium, paving the way for improved calcium batteries.

1. Introduction

Multivalent battery technologies based on alkali-earth metal anodes have emerged as a promising alternative to replace/complement today's dominant lithium-ion battery (LIB) technology, alleviating some inherent problems connected with resources, value chains, and performance [1–4]. Magnesium and calcium metal anodes possess very high capacities, much higher than the graphite anodes commonly used in LIBs, and are reasonably comparable to lithium metal anodes [5–10]. Additionally, these metals are much less prone to dendrite formation [11–13], but the layers that form on these metals in organic solvents are very stable and do not generally allow for any fast ion migration and/or diffusion [14–16]. To develop multivalent metal batteries, allowing for reversible deposition/stripping reactions, it is thus necessary to carefully design an electrolyte to enable tailoring of the surface layers formed.

Overall, the progress of multivalent metal batteries is more visible for magnesium batteries [13, 17–20]. For calcium electrodes, an electrochemical study using different organic electrolytes, $Ca(ClO_4)_2$ and $Ca(BF_4)_2$ in several commercially available organic solvents, carried out by Aurbach *et al* in 1991 [21] showed that the reactions were surface-film controlled, leading to very poor coulombic efficiencies and

making calcium deposition impossible, even at high overvoltages. Since then, many different electrolytes have been tested for the formation of calcium-ion permeable layers on negative electrodes [5]. To complicate matters, the low electrochemical potential of calcium, much closer to that of lithium than magnesium, renders spontaneous decomposition of salts and/or solvents [6]. However, the structure and properties of the passivating layers formed by these reactions are still not understood at a sufficiently detailed level. Albeit at low coulombic efficiencies, calcium deposition and stripping were achieved using $Ca(BH_4)_2$ in tetrahydrofuran [22] and $Ca(BF_4)_2$ in ethylene carbonate: propylene carbonate (EC:PC) electrolytes [23]. For the former, a significant amount of CaH_2 was identified on the calcium metal anode, while for the latter, CaF_2 was formed.

None of these electrolytes, however, offers the potential to be used in practical applications: BH_4^- is a strong reductant and its role is complicated by expected side reactions, especially on the positive electrode, and for the latter electrolyte, calcium deposition and stripping were obtained only at elevated temperatures ($\approx 100~^{\circ}$ C). Further studies revealed that some components, either pre-deposited on the calcium electrode surface or present in the electrolyte during cycling, can facilitate Ca^{2+} diffusion and thereby increase the coulombic efficiency [24]. This further highlights the sensitivity of the reactions toward the structure being created and, consequently, the Ca^{2+} permeation ability.

After these initial and partially successful attempts, further studies have been made to find a suitable electrolyte to enable facile calcium deposition and stripping [25, 26]. These studies were, however, hampered by the scarcity of commercially available calcium salts. In-house Ca-salt synthesis efforts have therefore been conducted, rendering, for example, relatively high coulombic efficiencies of up to 90% by using a 0.5 M calcium tetrakis(hexafluoroisopropyloxy) borate, $Ca[B(hfip)_4]_2$, in a dimethoxyethane electrolyte [26]. $[B(hfip)_4]^-$ is a large anion with very low nucleophilicity, and this aligns very well with the notion that the formation of the layer at the anode and the permeation ability depend not only on the structure of the layer itself but also on the Ca^{2+} solvation and ion pairing in the electrolyte [27–29]. More recently, calcium dodecaborate ($CaB_{12}H_{12}$) [30] and calcium tetrakis(hexafluoroisopropyloxy) aluminate, $Ca[Al(hfip)_4]_2$ [31], electrolytes have demonstrated reversible plating/stripping behavior on calcium and stainless steel (SS) electrodes, respectively. Other routes would be to perform an artificial Ca^{2+} permeable layer, for example, by electrolyte additives, such as BF_3 , which impact the interphase structure [32, 33].

Despite the progress made, obtaining effective calcium deposition and stripping remains challenging. The key factor missing is a proper understanding of the electrochemical processes occurring during charge/discharge, including the mechanism(s) and kinetics of any interphase formation, which is needed to establish a relationship between the properties of the layer and the Ca²⁺ permeability [34, 35].

Herein, we report on our progress using a Ca(BF₄)₂ in acetonitrile (ACN) electrolyte based on preliminary investigations showing favorable calcium deposition/stripping even at high cathodic potentials. ACN has some excellent properties with respect to its use as a battery and supercapacitor electrolyte solvent: relatively high salt concentrations can be achieved, due to its high dielectric constant, and together with its low viscosity/high fluidity, this can render very high ionic conductivities, often superior to other organic electrolytes [36, 37]. However, as it does not form a stable solid electrolyte interphase (SEI) on graphite [38], it has been investigated relatively scarcely for LIBs [39, 40], and this is true for calcium batteries as well [21, 41]. Another key drawback of ACN is its reductive instability, preventing its use in LIBs and other post-lithium technologies unless some strategies are taken to extend its electrochemical stability window [42, 43].

Therefore, with a focus on the calcium/ACN interface, and especially calcium metal electrodes using $Ca(BF_4)_2$ in ACN electrolytes, our goal was to determine how the electrolyte salt and solvent(s) affect the electrochemistry, structure, and properties of the layer created, and ultimately to create a basis for a structure–activity relationship between the electrolyte composition and Ca^{2+} permeability. For this purpose, we herein compare three electrolytes: $Ca(BF_4)_2$ and $Ca(TFSI)_2$ in ACN, and $Ca(BF_4)_2$ in EC:PC. We demonstrate that the presence of Ca salts hinders reductive decomposition of ACN at the calcium electrode, extending the negative potential range high enough to enable calcium deposition/stripping. The deposition reaction is governed by the structure of the formed inhibiting layer, which is highly sensitive to the anion present in the electrolyte. The results obtained allow us to understand the processes that govern the formation of passivating layers on the calcium metal negative electrode and pave the way for better reversibility and, ultimately, calcium batteries.

2. Experiment

2.1. Electrode and electrolyte preparation

All electrode and electrolyte preparation was done inside an argon atmosphere glovebox (VIGOR, SG1200 model) with H_2O and O_2 contents < 0.1 ppm. Calcium electrodes were prepared by pressing calcium

granules (Alfa Aesar, 99.5%, mesh 6) with a hydraulic press at a pressure of 20 bar, which were subsequently cut into a circular shape with a diameter of 0.64 mm and a thickness of 0.4 mm and polished with different grades of polishing pads, varying from 100 to 1200 grit sizes. SS disc electrodes (GoodFellow, 316 l) were polished using the same procedure as for calcium.

Ca(BF₄)₂ (TermoFischer Scientific, hydrate) and Ca(TFSI)₂ (Solvionic, 99.5%) were dried using a vacuum oven (Raypa, DAF-78, Spain) for 48 h at 120 °C to reduce water content to a level <100 ppm, as determined by Karl-Fischer titration. ACN (Fischer Chemical, HPLC grade), EC, and PC (both Sigma Aldrich, anhydrous) were dried with 3 Å molecular sieves (Alfa Aesar) for two weeks before being used and were stored in a glovebox. Electrolytes were prepared by dissolving Ca(BF₄)₂ or Ca(TFSI)₂ in ACN or EC:PC (50:50 by volume) by stirring overnight to render 0.5 M electrolytes.

2.2. Electrochemical characterization

All electrochemical measurements were performed on a Biologic VMP-3e potentiostat in a three-electrode Swagelok cell assembled inside the Ar glovebox. The Swagelok cells were assembled in a sandwich-like structure containing calcium or inert electrodes, either SS or Pt as the working electrode (WE) ($A = 0.31 \, \mathrm{cm}^{-2}$), active carbon as a counter electrode (CE), and platinum as a pseudo-reference electrode (RE). Glass fiber (EL CELL) was used as a separator and was soaked with 160 μ l cm⁻² of the electrolyte.

Open-circuit potential (OCP) measurements were performed on the calcium electrodes for 60 h, immediately after assembling the cell, and they were paired with electrochemical impedance spectroscopy (EIS) conducted in the frequency range from 1 MHz to 10 mHz with a 10 mV amplitude. Cyclic voltammetry (CV) was carried out using calcium and SS electrodes and varying potential ranges within –4.5 V to 1.5 V versus Pt (–1.3 V to 4.5 V versus Ca²⁺/Ca), depending on the experiment, with a scan rate of 10 mV s⁻¹. All potentials quoted in this paper are referred to the Ca²⁺/Ca standard reduction potential, which was obtained by determining the reduction potential of the ferrocenium/ferrocene (Fc⁺/Fc) redox couple on the Pt electrode versus a Pt pseudo-RE and assuming that the standard reduction potential of Fc⁺/Fc is 400 mV on the normal hydrogen scale [44] and is insensitive to the solvent/electrolytes. However, the experimental conditions are far from the standard state, and the Ca²⁺/Ca potentials should not be interpreted as absolute. The stability of the potential of the Pt pseudo-RE during prolonged experiments was checked by determining the difference in reduction potentials of the Fc⁺/Fc redox couple before and after a 24-hour OCP experiment. The shift was negligible. The results are available on request.

The electrochemical quartz crystal microbalance (EQCM) measurements used a SEIKO EGG QCM model 922 with a resonance frequency of 9 MHz, connected to the BioLogic VMP-3e potentiostat. A flow cell (Biologic, 092-QCA-FC) was assembled in the Ar glovebox and consisted of a quartz/SS WE and two Pt wires as the CE and RE. For mass change determinations, the Sauerbrey equation was used ($\Delta f = -C_f \Delta m$), where Δf is the quartz crystal oscillation frequency change, Δm is the corresponding mass change, and C_f is Sauerbrey's constant (Hz μg^{-1}). The linearity and accuracy of the Sauerbrey equation hold for fixed solutions [45].

The calibration of the EQCM was made using the slope of the linear portion of the frequency change versus the charge passed during the electrochemical deposition of Ag⁺ from an ACN solution. From the equation

$$C_{\rm f} = \frac{{\rm Slope} \cdot F}{M_{\Delta_{\alpha}}},\tag{1}$$

the determined sensitivity was 9.09 Hz μ g⁻¹ or 0.11 μ g Hz⁻¹.

All measurements above were done at least in triplicate.

2.3. Physical characterization

After the electrochemical measurements, the Swagelok cells were disassembled inside the glovebox. The calcium and SS electrodes were carefully recovered from the sandwich structure and washed with the corresponding solvent.

Fourier transform infrared (FTIR) spectra were taken on a Shimadzu IRTracer-100 (Shimadzu, Kyoto, Japan) spectrometer with an attenuated total reflectance (ATR) attachment in the range of 400–4000 cm⁻¹ and a resolution of 0.5 cm⁻¹.

X-ray diffraction experiments were conducted using a D8 Advance (Bruker, Billerica, USA) diffractometer with $\text{CuK}\alpha$ radiation at an acceleration voltage of 40 kV and 30 mA of current in a grazing incidence configuration, with a continuous-scan mode where the steps were set to 0.02 °2 θ , in the range of 20–80 °2 θ with a counting time of 3 s and with an α incidence angle of 0.25°. The surface morphology of the SS electrodes was examined using scanning electron microscopy (SEM) with a Tescan Vega III Easyprobe instrument (Tescan Orsay Holding, Brno, Czech Republic) at a working distance of approximately 8 mm and an acceleration voltage of 10 kV.

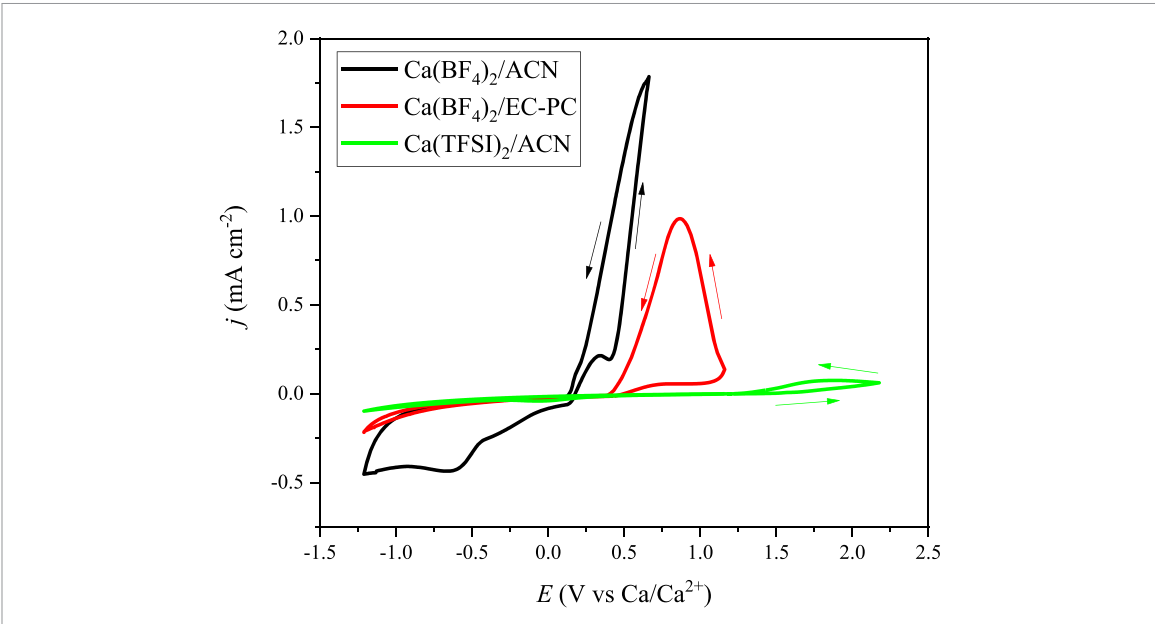


Figure 1. CVs of calcium electrodes in the three different electrolytes: $Ca(BF_4)_2$ (black), $Ca(BF_4)_2$ (red), and $Ca(TFSI)_2$ (green). Scan rate: 10 mV s^{-1} .

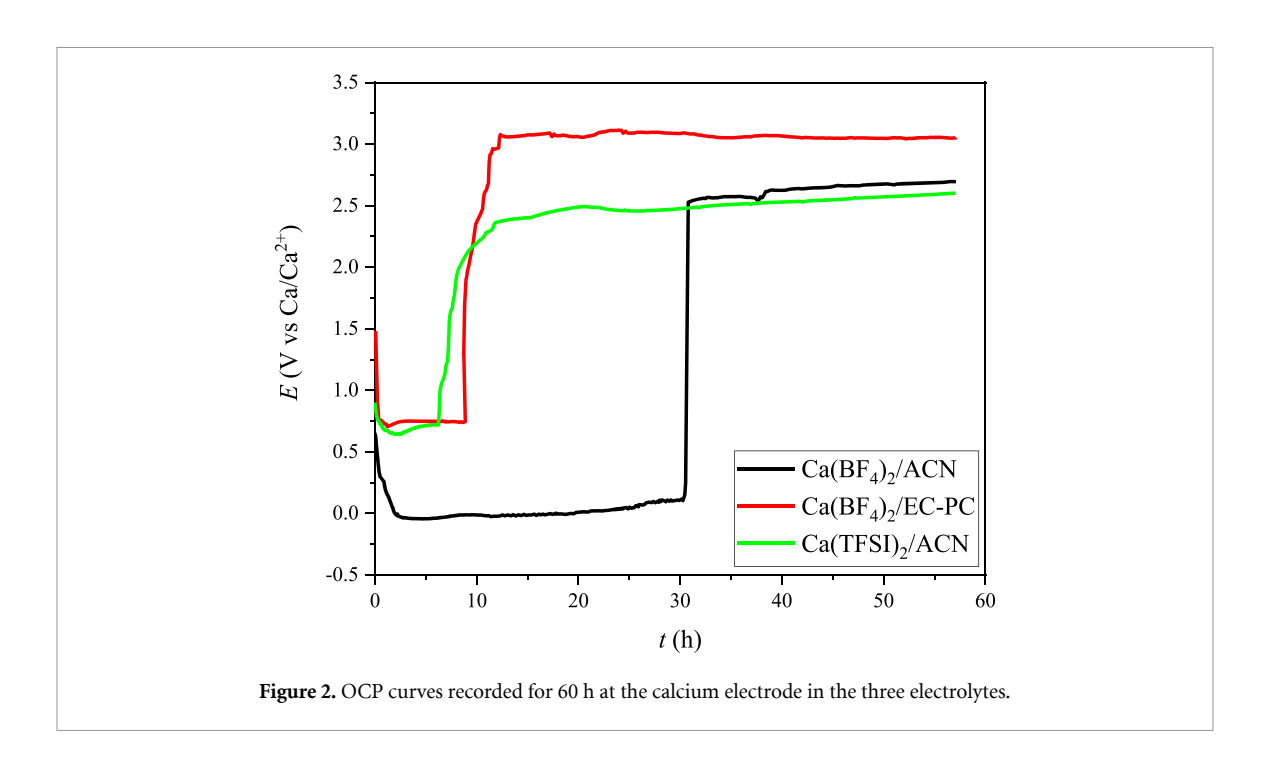
3. Results and discussion

First, we demonstrate the importance of electrolyte composition for the electrochemistry of calcium electrodes, particularly for passivating layer formation and calcium deposition/stripping reactions, by using three different solvent/salt combinations. Second, we use the same electrolytes, but avoid the possible complications with pre-formed passivating layers on the calcium by using an SS inert electrode for the calcium plating. Finally, we carefully characterize the electrode surfaces and layers formed by *ex situ* microscopic and spectroscopic techniques.

3.1. Electrochemistry using calcium electrodes

The CVs of calcium electrodes immersed in our three different electrolytes clearly show that the electrochemical behavior is quite different (figure 1). In all cases, the cathodic deposition of calcium is hindered compared to its anodic stripping counterpart, with significantly higher anodic currents observed, indicating that they are governed by different mechanisms. While the cathodic plating is preceded by diffusion of Ca²⁺ through the formed low-permeability passivation layer as a rate-determining step, the anodic stripping disrupts the passivation layer and proceeds without hindrance. Furthermore, the anodic current hysteresis demonstrates calcium's strong tendency to undergo pitting attacks, resulting in the breakdown of passivation layers. The critical pitting potential, indicated as the onset of the anodic current rise, reflects the protective properties of the passivating layer toward the pitting attack. Hence, the passivating layer formed using the Ca(TFSI)₂ in ACN electrolyte has the best protective properties, with its critical pitting overvoltage being 1.5 V higher compared to the $Ca(BF_4)_2$ in EC:PC electrolyte at approximately 1.0 V. Surprisingly, the Ca(BF₄)₂ in ACN electrolyte has a very low anodic overvoltage, leading to intense stripping of calcium, which probably occurs as a combination of a uniform dissolution and simultaneous formation of pits. In this case, either a passivating layer was not formed at all or, if formed, had no protective properties. Uniform dissolution of calcium seems reasonable since the increase in the anodic current coincides with the pitting protection potential (the potential at which backward cathodic excursion crosses the current axis).

The most striking features in figure 1 are the suppression of the ACN reductive decomposition in these electrolytes and the appearance of a Ca^{2+} reduction peak and concomitant calcium deposition only for the $Ca(BF_4)_2$ in ACN electrolyte. As demonstrated by the comparison of cathodic currents in $Ca(BF_4)_2$ and tetraethylamino tetrafluoroborate (TEABF₄) electrolytes in figure S1, the ACN reduction current is clearly suppressed in Ca^{2+} -based electrolytes, and, furthermore, depending on the electrode and conditions, one or more new reduction peaks appear. The reason for this is not quite clear, but as the inhibiting layer on Ca forms as soon as the electrode is immersed in the electrolyte, this prevents ACN from further degrading. There was no yellow miscoloration of the separators for any of the electrolytes (and hence no degradation of ACN, possibly causing HCN formation), as has been observed versus Li metal. The cathodic currents in $Ca(BF_4)_2/ACN$ are approximately ten times higher than in other electrolytes, and thus diffusion of calcium



ions through the passivating layer does not seem to be a limiting step. This indicates a strong sensitivity of the structure and properties of inhibiting layers formed on calcium to the solvent/electrolyte composition. The electrochemical processes observed are not reversible, but their repeatability was investigated by cycling through five consecutive cycles. The results can be found in the supplementary information (figures S3–S5). The high sensitivity of the results to the electrolyte composition is also supported by a recent paper by Biria $et\ al\ [46]$, who demonstrated that reversible plating and stripping of calcium on a Cu substrate at room temperature in Ca(BF₄)₂/EC:PC at high efficiencies over several cycles is possible.

To gain a deeper insight into the processes that govern the electrochemical reactions at the calcium electrode in these three electrolytes, the OCP was monitored, accompanied by EIS at regular time intervals (figure 2). As calcium electrodes readily corrode, it might be more appropriate to use the term corrosion potential (Ecorr) rather than OCP. However, there is fundamentally no big difference between the OCP and Ecorr concepts in reality. The difference is slight and mainly connected to the study area and not the methodology. All OCP curves follow a similar pattern: after an initial drop, there is a sudden final jump to high positive potentials. In the latter region, the electrodes are completely passivized, impedance modules are in all cases extremely high (not shown), and no further electrochemical reactions at the calcium electrode are possible, at least not to any appreciable extent. The initial potential drop and the time to reach the steady-state regions, as well as their length, all depend on the electrolyte used. The OCP curves for the Ca(BF₄)₂ in EC:PC and Ca(TFSI)₂ in ACN electrolytes exhibit similar characteristic features. The corrosion potential in the steady state is almost identical, and the time required to reach complete passivation is similar, while the features of the OCP curve for $Ca(BF_4)_2$ in ACN differ. The length of the induction period is approximately 9 h, and the corrosion potential is more negative than in the other two cases, approaching 0 V versus Ca²⁺/Ca. This means that the passivation layer does not protect the calcium electrode as well as in the Ca(BF₄)₂ in ACN electrolyte, and that its potential needs to counteract the strong tendency of calcium to dissolve by shifting toward more negative values to reach equilibrium. In stark contrast, a more negative corrosion potential and a much longer steady-state region (30 h) are signs that we have a synergy for only this salt and solvent combination, activating the calcium electrode.

To follow the change in the properties and structure of the calcium/electrolyte interfaces in these three electrolytes, EIS was taken at regular time intervals during the initial OCP period and in the steady-state region. The Nyquist plots for $Ca(BF_4)_2$ in ACN (figures 3(a) and (b)) show that the impedance modulus decreases during the initial OCP period (figure 3(a)), reaches a minimum, and then starts to increase again (figure 3(b)).

All three electrolytes follow this trend, but the time required to reach the minimum impedance is longer for the other two electrolytes. The absolute impedances of the other two electrolytes are higher than the impedances of $Ca(BF_4)_2/ACN$ (figure 3(c)), which is in agreement with both the CV and OCP analyses.

A first inspection of the impedance data reveals that, at OCP, the Ca/electrolyte interface goes through at least three competing processes, one being a charge transfer leading to uniform or pitting dissolution of

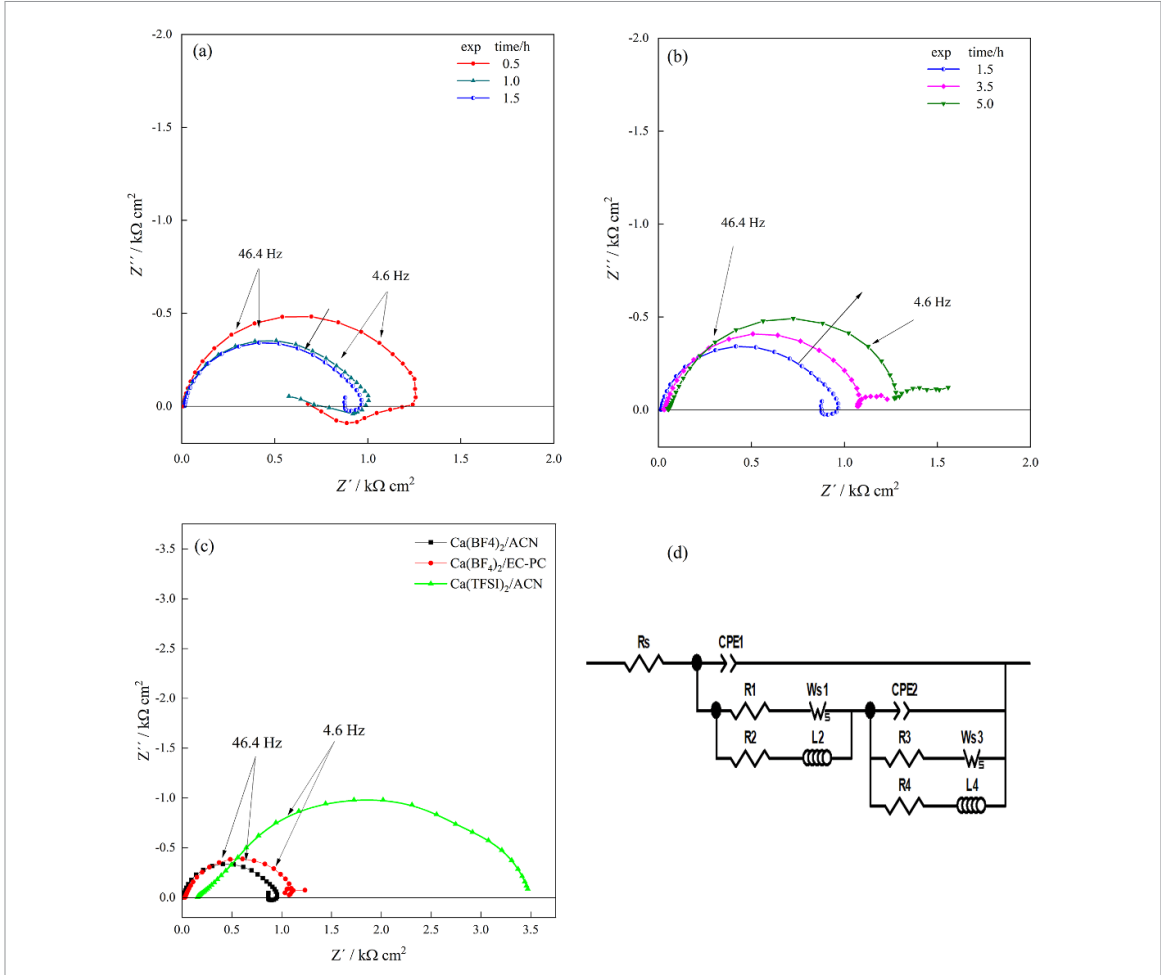


Figure 3. Time evolution of Nyquist plots for calcium electrodes in the $0.5 \text{ M Ca}(BF_4)_2$ in ACN electrolyte: (a) during the first 1.5 h, (b) from 1.5 to 5 h, at OCP, (c) Nyquist diagrams obtained for all three electrolytes at minimum impedances, and (d) the equivalent circuit used to fit the experimental data.

calcium. The other two processes tend to inhibit the charge transfer reaction. These impedance data can be explained by the formation of at least two different passivating layers. The formation of the first passivating layer is fast; it takes place immediately after or during calcium deposition. This layer is unstable for some reason, probably because the competing calcium dissolution at the corrosion potential counteracts its formation and prevents further growth. The inductive loop in the low-frequency region, a common characteristic of corrosion processes, especially those in the presence of inhibitors or those involving pitting, supports this hypothesis.

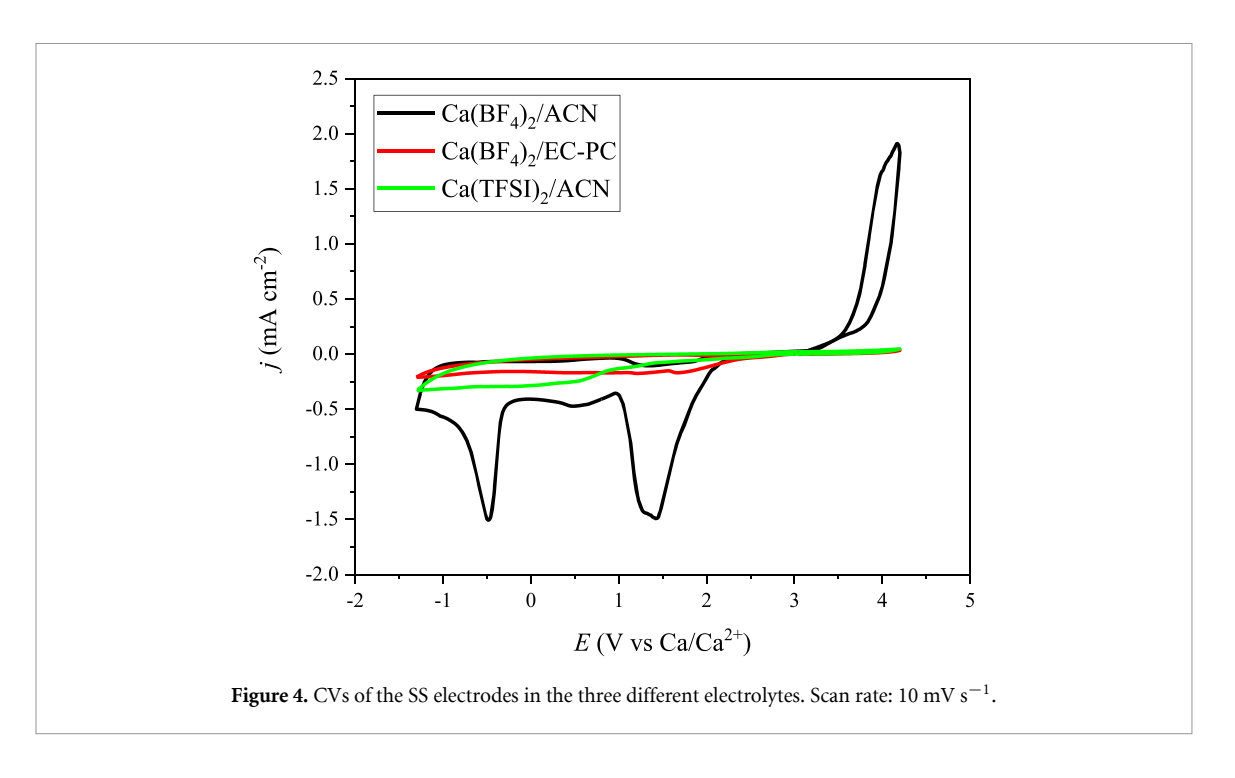
As a result, the impedance of the calcium electrode initially decreases. The initial passivating layers formed in the other two electrolytes are obviously different, which are much more stable and/or the charge transfer resistance is much higher. The existence of these two types of passivation layers has recently been confirmed by Lin *et al* [47], who reported the formation of two distinct layers on calcium at OCP. The native passivation layer, referred to as the first layer, promotes calcium reversible plating/stripping primarily due to the formation of the organic-rich SEI, creating a porous, activated Ca surface. Over prolonged exposure of the calcium electrode to the same electrolyte, the electrolyte starts to penetrate through the native layer, causing the formation of the second layer.

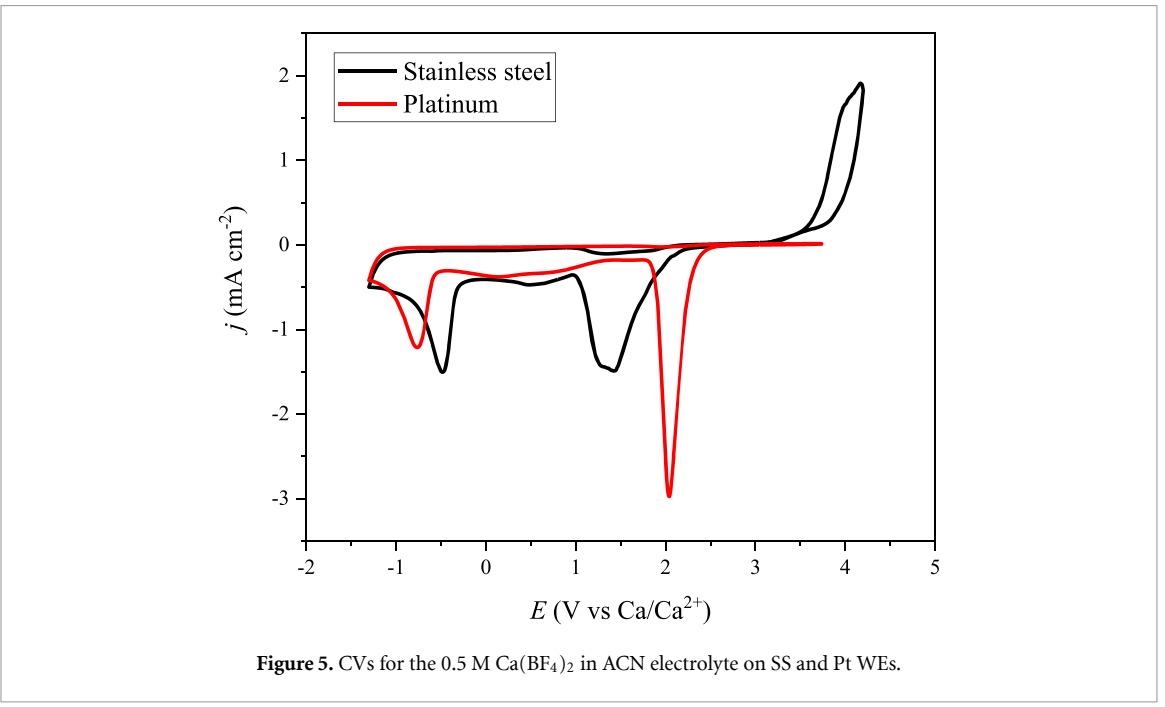
Figure 3(d) shows the equivalent circuit used to model the impedance data. It consists of two parallel circuits. The first circuit describes the changes resulting from the destruction of the first layer, while the second circuit represents the formation and electrical properties of the second layer, whose impedance increases with time.

The complete analysis of the impedance data is the subject of our following paper.

3.2. Calcium deposition and stripping on SS electrodes

The CVs of calcium deposition/stripping on SS in Ca^{2+} -based electrolytes are in accordance with those obtained on calcium, in that the ACN reductive decomposition is suppressed (figure S2) and calcium deposition occurs at appreciable rates only for the $Ca(BF_4)_2$ in ACN electrolyte (figure 4). Here, as soon as





the first calcium deposits are formed, the electrode starts to behave like a Ca electrode, stabilizing the ACN. Again, in the other two electrolytes, the reaction is inhibited due to the fast formation of low-permeable passivating layers, while, when using the $Ca(BF_4)_2$ in ACN electrolyte, either the passivating layer does not form or its permeability for Ca^{2+} is sufficiently high.

An even more striking difference between the $Ca(BF_4)_2$ in ACN electrolyte and the other two electrolytes is the existence of a sharp reduction pre-peak at very high positive potentials at approximately 1.5 V versus Ca^{2+}/Ca . This peak also appears when Ca is deposited on Pt (figure 5). The pre-peak involves calcium reduction and deposition since calcium stripping occurs at its characteristic potentials even when the cathodic excursion is shortened and reversed just after the pre-peak (figure 6). The anomaly of these results suggests either unconventional interfacial chemistry or potential experimental artifacts, such as those observed for current collector corrosion [48] or inorganic-rich SEIs derived from an aggregate-dominated electrolyte [49]. However, a more reasonable explanation is that the electrodeposition of calcium on SS and Pt occurs either as a mediated process involving ACN as an electron transfer mediator or via underpotential deposition (UPD). The argument for the former is the close resemblance of the registered current peak

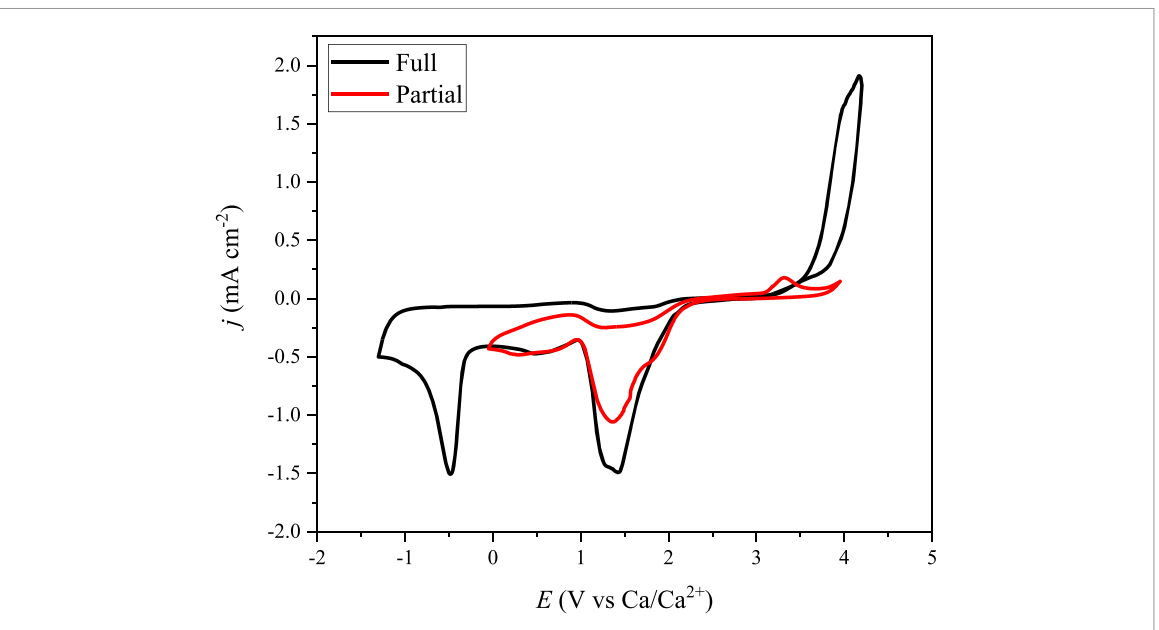


Figure 6. Cyclic voltammograms for the $0.5 \text{ M Ca}(BF_4)_2$ in ACN electrolyte on an SS electrode before and after shortening of the final cathodic potential.

potential and the ACN reduction potential (figure S2). In this case, different forms of calcium-containing organic layers derived from ACN reduction products should/could be envisaged. On the other hand, UPD is a phenomenon well known for metallic deposition on foreign substrates and other reactions involving the adsorption of intermediates, such as the hydrogen evolution reaction. The difference between the thermodynamic reduction potential of calcium and the observed potential of the reduction peak excludes mediated electron transfer assignment, as this affects the electron transfer kinetics, but not its thermodynamics. During UPD, metallic deposition takes place at potentials that are more positive than the thermodynamic reduction potentials. It reflects a difference in the adsorption free energies between the bonding of the atoms of the same metal, M-M, and different metals, M-S [50]. In our case, the calcium UPD potentials are very high, with apparent values in the range 1.5-2.0 V, depending on the substrate. Accurate potential values would be challenging to estimate due to the uncertainty in determining the thermodynamic potential scale in organic electrolytes. The calcium potential scale, which is frequently used to display voltammetric data in published papers [22, 24, 26, 51], regardless of how it was determined, by using a Ca-metal pseudo-RE or calibrating through the Fc⁺/Fc redox couple, might be subject to large errors and erroneous interpretations. The UPD peak of Ca on Pt is sharper and shifted for an additional \sim 0.5 V toward more positive potentials than the peak on SS. SS is an alloying material consisting of several different active sites available for deposition, and most probably the different adsorption energies cause the peak widening. A UPD peak also appears using the other two electrolytes (cf. the EQCM data), but the overall current is much smaller and quite negligible in comparison, again supporting that the passivating layers are not permeable to Ca²⁺ ions to any considerable extent.

The repeatability of cyclic voltammograms obtained at the SS electrode was investigated through five consecutive cycles, and the results are displayed in the supplementary information, figures S6–S8.

The current does not drop to zero after the UPD peak, as might be expected if there were a monolayer formation of metal on the foreign substrate. Undoubtedly, the calcium deposition proceeds at more negative potentials until the overpotentials of calcium deposition on the calcium substrate are reached, where it forms the expected calcium reduction peak in resemblance to the deposition directly on a Ca substrate. The calcium deposition after the UPD peak can be explained by the continuous corrosion process of calcium, liberating the substrate surface, which becomes available for further calcium deposition. If true, then the currents in the region between the two peaks reflect the rate of corrosion and the dissolution of pre-deposited calcium.

More detailed insights into the mechanism of interfacial reactions can be obtained by following mass changes during electrochemical deposition and stripping with EQCM. The CVs and corresponding EQCM frequency changes for the calcium deposition on the SS electrode (figures 7(a), (c), and (e)) show that the frequency decrease and consequently mass increase are observed from the foot of the UPD waves up to the final cathodic scanning potential. In the reverse oxidation direction, the frequency remains constant for ACN electrolytes, while for the EC:PC electrolytes, the mass continues to increase even in the reverse scan, signifying that calcium deposition continues as a thermodynamically irreversible reaction.

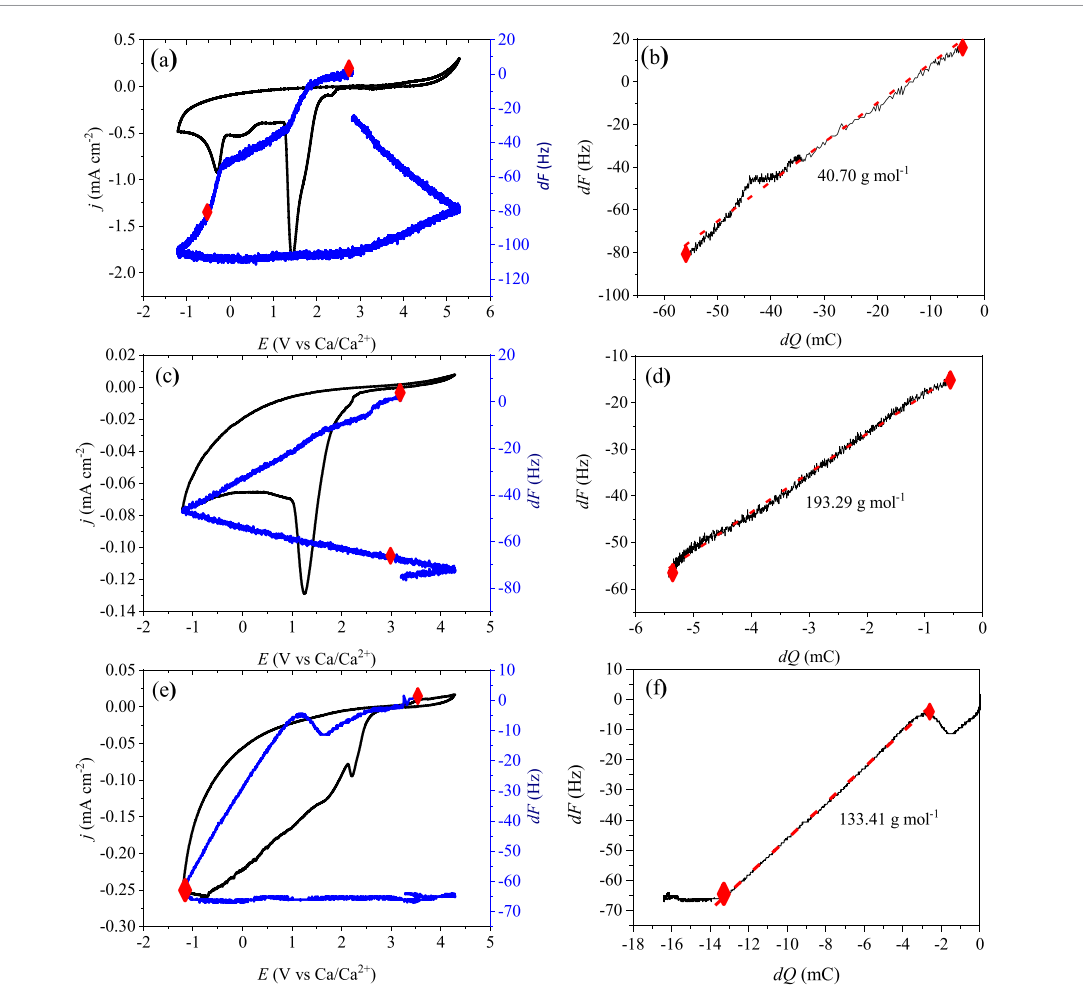


Figure 7. Results of EQCM on the SS electrode: (a) CV and frequency change with potential of the 0.5 M Ca(BF₄)₂ in ACN electrolyte, (b) $\Delta m/\Delta Q$ dependence on charge change for the selected region of CV for the 0.5 M Ca(BF₄)₂ in ACN electrolyte, (c) CV and frequency change with potential of the $Ca(BF_4)_2$ in EC:PC electrolyte, (d) $\Delta m/\Delta Q$ dependence on charge change for the selected region of CV for the 0.5 M Ca(BF₄)₂ in EC:PC electrolyte, (e) CV and frequency change with potential of the 0.5 M Ca(TFSI)₂ in ACN electrolyte, and (f) Δ m/ Δ Q dependence on charge change for the selected region of CV for the 0.5 M Ca(TFSI)2 in ACN electrolyte.

As a complement, figures 7(b), (d), and (f) represent the Δf versus ΔQ relationship derived from the corresponding Δf versus E plots (figures 7(a), (c), and (e)), which is helpful since they enable the determination of the molar masses of the species, participating in the deposition and/or dissolution. A linear region of Δf versus ΔQ plots is observed in all cases for the reaction in a relatively large potential window, indicating a simple reaction step involving a single species deposited on the electrode. The linearity of the $\Delta f/\Delta Q$ change and consequently of the $\Delta m/\Delta Q$ change spans almost the whole cathodic region of the cyclic voltammograms, as marked by the red dots on the figures. In the presence of the TFSI anion, the linearity involves the whole cathodic and anodic region where the mass increase occurs. From the slope of the linear segments, the molar masses of the deposited species can be calculated according to the equation

$$M_W = \frac{S \cdot z \cdot F}{C_{\rm f}} \tag{2}$$

where S is the slope of linear segments on the $\Delta m/\Delta Q$ plots, z is the number of exchanged electrons (n=2for calcium deposition), Fis the Faraday constant, and C_f is the sensitivity of EQCM as described in the experiment section ($C_f = 0.11 \,\mu g \, Hz^{-1}$).

The calculated molar mass for the $Ca(BF_4)_2$ in ACN electrolyte is 40.70 g mol⁻¹, almost exactly the same as the molar mass of calcium (40.08 g mol⁻¹). For the other two electrolytes, the molar masses of the deposited species are much higher: 193.3 and 133.4 g mol⁻¹ for Ca(BF₄)₂ in EC:PC and Ca(TFSI)₂ in ACN,

These results align well with other results described in this paper, demonstrating that calcium deposition is favorable for the Ca(BF₄)₂ in ACN electrolyte and that no insoluble products other than calcium are simultaneously deposited on the electrode. However, these results should be approached with caution since it

Figure 8. SEM micrographs of the surfaces of the SS electrodes after the deposition of calcium from: (a) $0.5 \text{ M Ca}(\text{TFSI})_2$ in ACN, (b) $0.5 \text{ M Ca}(\text{BF}_4)_2$ in EC:PC, (c) $0.5 \text{ M Ca}(\text{BF}_4)_2$ in ACN at -1.0 V, and (d) $0.5 \text{ M Ca}(\text{BF}_4)_2$ in ACN at 1.0 V.

would be easy to identify other products derived from the mediated electron transfer deposited on the electrode with similar molar masses to calcium. As the molar mass of ACN is similar to the molar mass of calcium, the observed value could also be ascribed to any combination of [CH₂CN–Ca] species. It is reasonable to assume that the processes occurring at the first current peak involve a combination of SEI formation and calcium deposition. The results for the other two electrolytes show that, during or immediately after calcium deposition, a solvent and/or salt is simultaneously decomposed, covering the deposited calcium and passivating its further deposition to a greater or lesser extent.

3.3. Physical characterization of the layers obtained on SS electrodes

There is also further evidence confirming that the nature of the pre-peak involves the reduction/deposition of calcium. Figures 8(a)-(d) show SEM micrographs of the SS electrode surfaces after Ca deposition from the three electrolytes, while figures 9(a)–(d) provide the corresponding energy dispersive X-ray spectroscopy (EDS) spectra. The SEM micrographs of the SS electrode surfaces after Ca deposition after the pre-peak (E = 1.0 V) (figure 8(d)) and after Ca deposition after the second cathodic peak (E = -1.0 V) (figure 8(c)) show that, in both cases, clusters assigned to deposited calcium or its corroded products are observed. The corresponding EDS spectra focusing on the deposited clusters (circled areas) (figures 9(c) and (d)) confirm that these consist of metallic calcium, at least partially. The calcium content in the $Ca(BF_4)_2$ in ACN electrolyte area was 28.7%, while the fluorine content was 44%, indicating the formation of CaF₂. The chromium and the iron originate from the SS electrode (figure 9). A complete chemical analysis of the EDS spectra is given in tables S1-S4 in the supplementary information. The SEM micrographs taken for the other two electrolytes (figures 8(a) and (b)) did not show any new features on the surface of the SS, except for the polishing abrasion on the surface, regardless of the calcium deposition potential and deposition time. Although the SEM micrographs do not show any specific features that could be assigned to calcium deposition, the CV results show calcium oxidation, indicating that metallic calcium was present on the surface of the SS. These observations support the conclusions drawn from EIS data that calcium deposition goes through at least two processes, which oppose calcium corrosion. The first process involves the formation of thin and compact passivating layers on the electrodes for the Ca(BF₄)₂ in EC:PC and Ca(TFSI)₂ in ACN electrolytes, while for the Ca(BF₄)₂ in ACN electrolyte, the layer also forms, but, in contrast, does not hinder further calcium deposition. A thin and compact layer of calcium-solvent degradation products is also supported by the SEM/EDS results for the pristine SS surface with no calcium signal (figures S9 and S10).

The x-ray diffraction (XRD) spectra of the SS samples after calcium deposition from three different electrolytes show that the $Ca(BF_4)_2$ in EC:PC and $Ca(TFSI)_2$ in ACN electrolytes do not add any additional phases on the surface of the SS electrodes (figure 10). On the other hand, the formation of some calcium species could be detected for the $Ca(BF_4)_2$ in ACN electrolyte experiment, where the species could be ascribed to Ca and its salts, possibly CaF_2 , corresponding to findings from the literature [24, 52]. The x-ray diffraction pattern does not fully confirm Ca metal deposition, as it could also be CaF_2 . Distinguishing Ca metal from CaF_2 would require synchrotron x-ray diffraction data [23]. It should be noted that the XRD spectra were taken ex situ on the SS samples after the 4 h prolonged electrodeposition at the potentials of the second cathodic current peak. The formation of the indicated species thus cannot be directly correlated with the EQCM results in figure 7, as these were obtained over a much shorter time frame.

The FTIR spectra of the calcium and SS electrode surfaces after the deposition of Ca show layers on the calcium obtained after the deposition from the three different electrolytes (figure 11(a)). All three spectra indicate the presence of organic compounds. At first sight, a clear difference in the intensity of the FTIR spectra can be observed. From the BF₄⁻-based electrolytes, peaks at 1070 cm⁻¹ and 769 cm⁻¹ correspond to B–F vibrations [53]. The major differences between these two electrolytes are the intensity of the peaks and

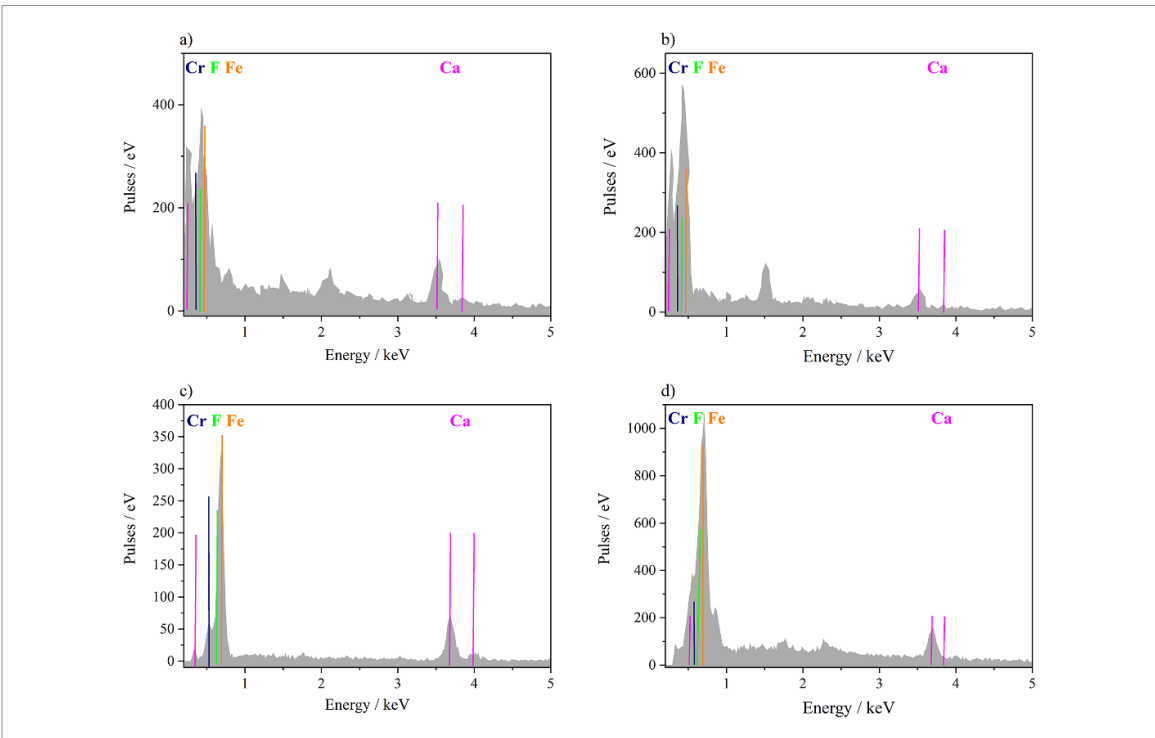
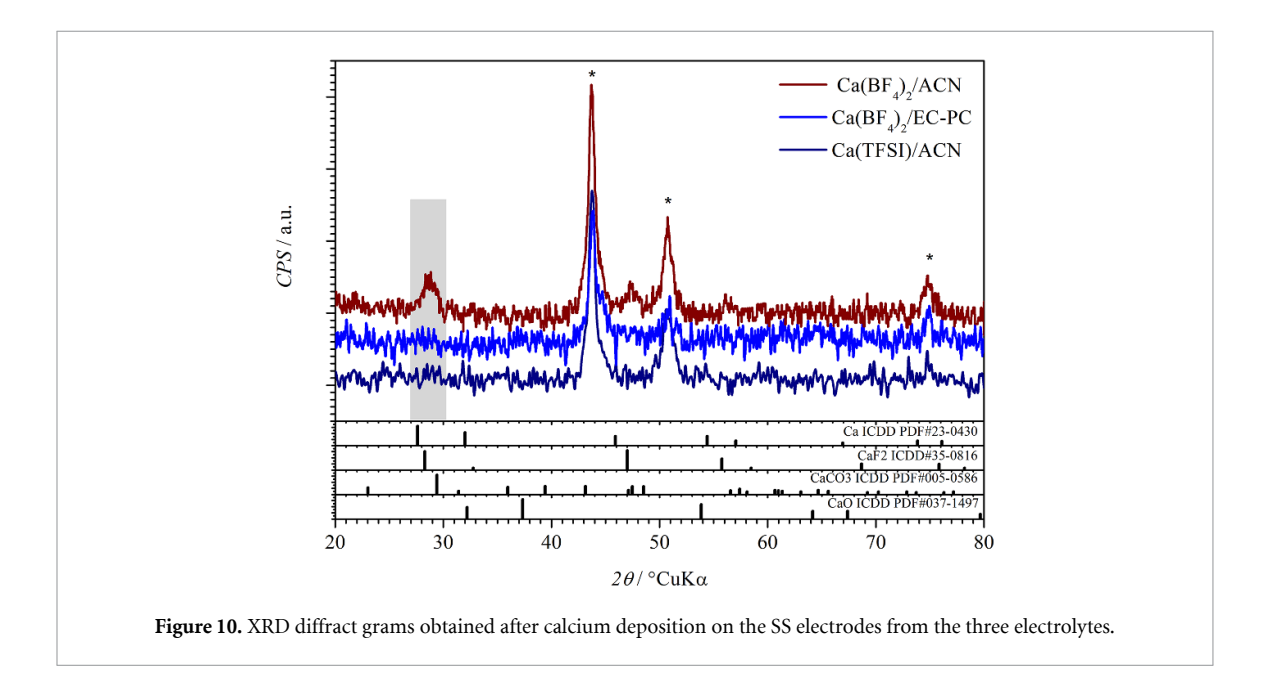


Figure 9. EDS spectrum of the circled part of the SEM micrographs: (e) 0.5 M Ca(TFSI)₂ in ACN, (f) 0.5 M Ca(BF4)₂ in EC:PC, (g) 0.5 M Ca(BF₄)₂ in ACN at -1.0 V, and (h) 0.5 M Ca(BF₄)₂ in ACN at 1.0 V.



the decomposition products of the electrolytes. In the case of carbonate-based solvents, the absorption of the carbonyl and C–O groups, at 1770 cm⁻¹ and 970 cm⁻¹, respectively, dominates the spectra. Other peaks can be assigned to the B–O group at 1390 cm⁻¹, and C–C and C–H stretch at 1480 cm⁻¹ and 1350 cm⁻¹, respectively. These groups may indicate the possible presence of ester, the carboxyl group, or anhydride compounds, as well as alkoxy and alkyl compounds inside the passivating layer [24]. As expected, the surface of the calcium deposited from CaBF₄ in ACN shows different functional groups: an N–H signal at 3640 cm⁻¹ and a C–N signal at 2300 cm⁻¹ [54]. Overall, the absorption peaks are of much lower intensity than those in the spectra obtained from the EC:PC electrolyte, which might indicate a thinner and loosely bound passivating layer. The TFSI-based electrolyte mainly shows signals of functional groups belonging to the TFSI anion in combination with N–H and C–N signals coming from ACN or its decomposition products.

A comparison of the FTIR spectra of the passivating layers formed on the SS electrode at the thermodynamic reduction potentials of Ca²⁺ and on the UPD potentials shows the presence of three major

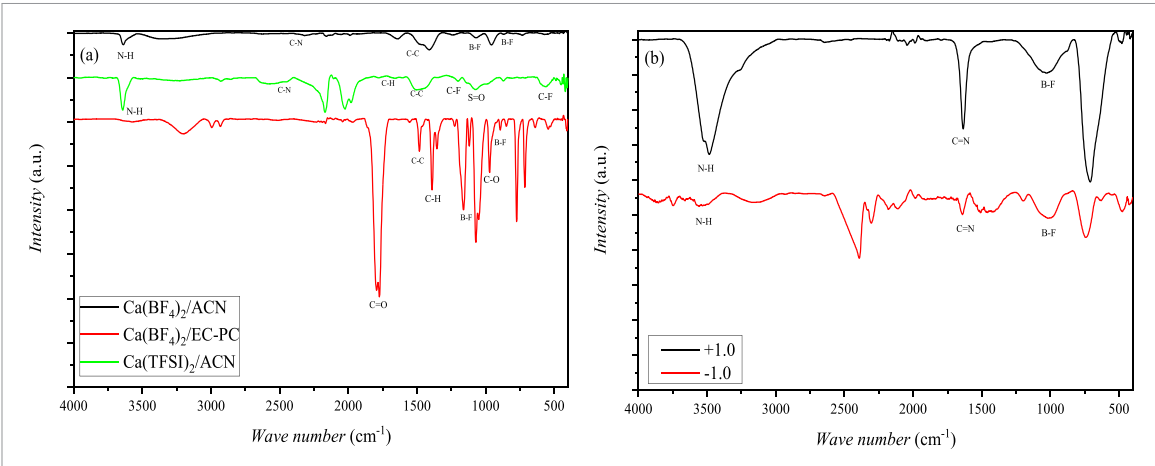


Figure 11. FTIR spectra of (a) calcium electrodes after deposition from the three electrolytes, and (b) the SS electrode at different polarization potentials: -1.0 V (red) and +1.0 V (black).

peaks (figure 11(b)), which correlate well with the spectrum obtained for the layers formed on the calcium electrode. The layers were formed by holding the SS electrodes for 4 h at the corresponding potentials before disassembling the cells. The direct correlation between the FTIR and other results obtained in this work in much shorter time frames cannot be directly correlated. The first is the B–F vibration at 1006 cm⁻¹, predominantly from BF₄. Next, the C=N signal at 1630 cm⁻¹ is usually assigned to the imide bond. In our case, this would mean that ACN reduces and participates in the formation of an organic SEI layer. The last signal, N–H, can be found at 3490 cm⁻¹, demonstrating the presence of an amine group inside the SEI layer.

4. Conclusions

A comparative study of calcium deposition/stripping in three electrolytes on calcium and SS electrodes indicates a large sensitivity of the mechanisms and kinetics of this reaction to the experimental conditions. Calcium deposition is enabled by suppressing ACN reductive degradation in the presence of Ca salts. The exact mechanism of this stabilization is not known, but it is related to the structure and composition of the resulting inhibiting layers. This points to the formation of a passivating layer as a major step in the formation of reversible calcium negative electrodes. On Ca electrodes, the lowest potential for calcium deposition was obtained in the Ca(BF₄)₂ in ACN electrolyte, followed by the Ca(BF₄)₂ in EC:PC electrolyte, while Ca(TFS)₂/ACN hinders the deposition reaction, which can then be achieved at very high overpotentials. The anodic reaction of calcium in these electrolytes indicates a corrosion process by pitting. Similar to calcium deposition, the rates of anodic dissolution governed by pitting depend on the electrolyte used. The calcium immersed in the Ca(TFS)₂/ACN electrolyte was most stable, while the rate of anodic dissolution was the highest for Ca(BF₄)₂ in ACN. Relatively low overpotentials of calcium deposition from the Ca(BF₄)₂ in ACN electrolyte and low anodic stripping potentials indicate a synergistic effect, enabling calcium deposition without hindrance compared to the other two salt/solvent combinations. The effects obtained in the other two electrolytes are much less pronounced. On the SS electrode, in addition to the main calcium reduction peak, there is also a pre-peak assigned either to mediated calcium reduction by ACN or the UPD of calcium. The reduction pre-peak is not well pronounced in the $Ca(BF_4)_2/EC:PC$ and $Ca(TFS)_2/ACN$ electrolytes. Although EQCM, SEM, and EDS measurements cannot unambiguously prove that there is calcium deposition on the potentials of the pre-peak, the oxidative peak in CVs when the reductive potentials excursion is shortened to the potentials immediately after the pre-peak indicates that some metallic calcium is formed at these potentials.

The EQCM measurements indicated the molar masses of the species deposited on the electrodes during the deposition of calcium from the three electrolytes. In the $Ca(BF_4)_2/ACN$ electrolyte, the molar mass is close to the molar mass of calcium metal. The molar masses differ depending on the electrolyte, indicating the complexity of the inhibiting layer formation. A major issue in the tailoring of calcium-permeable passivation layers is calcium corrosion, which readily occurs in all the electrolytes investigated. The results presented in this paper add to the existing knowledge of the electrochemical properties of calcium in organic electrolytes and might pave the way toward the realization of reversible calcium electrodes. However, a proper understanding of the mechanism and kinetics of electrochemical reactions at calcium electrodes is still required, and establishing the structure–activity relationship between the properties of the passivation layer and electrolyte composition is needed.

Data availability statement

The data cannot be made publicly available upon publication because they are not available in a format that is sufficiently accessible or reusable by other researchers. The data that support the findings of this study are available upon reasonable request from the authors.

Acknowledgment

We are grateful for the support from the NATO SPS Programme, which funded this research under Project Number SPS G5910. We thank dr sc. Krešimir Kvastek for his invaluable support and discussion of the EIS results.

ORCID iDs

Grgur Mihalinec © 0009-0008-2373-5735 Arijeta Bafti © 0000-0001-7343-1299 Patrik Johansson © 0000-0002-9907-117X Zoran Mandić © 0000-0003-4993-9396

References

- [1] Palacin M R et al 2024 Roadmap on multivalent batteries J. Phys. Energy 6 031501
- [2] Liang Y, Dong H, Aurbach D and Yao Y 2020 Current status and future directions of multivalent metal-ion batteries Nat. Energy 5 646–56
- [3] Ponrouch A, Bitenc J, Dominko R, Lindahl N, Johansson P and Palacin M R 2019 Multivalent rechargeable batteries *Energy Storage Mater.* 20 253–62
- [4] Biswal P 2023 Battery technologies: lithium & beyond: editorial J. Electrochem. Sci. Eng. 13 589–90
- [5] Deng X, Li L, Zhang G, Zhao X, Hao J, Han C and Li B 2022 Anode chemistry in calcium ion batteries: a review Energy Storage Mater. 53 467–81
- [6] Arroyo-de Dompablo M E, Ponrouch A, Johansson P and Palacín M R 2020 Achievements, challenges, and prospects of calcium batteries Chem. Rev. 120 6331–57
- [7] Wei Q, Zhang L, Sun X and Liu T L 2022 Progress and prospects of electrolyte chemistry of calcium batteries Chem. Sci. 13 5797–812
- [8] Hosein I D 2021 The promise of calcium batteries: open perspectives and fair comparisons ACS Energy Lett 6 1560–5
- [9] Chen C, Shi F and Xu Z-L 2021 Advanced electrode materials for nonaqueous calcium rechargeable batteries J. Mater. Chem. A 9 11908–30
- [10] Song H and Wang C 2022 Current status and challenges of calcium metal batteries Adv. Energy Sustain. Res. 3 2100192
- [11] Stolz L, Winter M and Kasnatscheew J 2023 Perspective on the mechanism of mass transport-induced (tip-growing) Li dendrite formation by comparing conventional liquid organic solvent with solid polymer-based electrolytes: original scientific paper J. Electrochem. Sci. Eng. 13 715–24
- [12] Pu S D et al 2020 Current-density-dependent electroplating in Ca Electrolytes: from globules to dendrites ACS Energy Lett. 5 2283–90
- [13] Muldoon J, Bucur C B and Gregory T 2014 Quest for nonaqueous multivalent secondary batteries: magnesium and beyond Chem. Rev. 114 11683–720
- [14] Forero-Saboya J D, Tchitchekova D S, Johansson P, Palacín M R and Ponrouch A 2022 Interfaces and interphases in Ca and Mg batteries Adv. Mater. Interfaces 9 2101578
- [15] Dugas R, Forero-Saboya J D and Ponrouch A 2019 Methods and protocols for reliable electrochemical testing in post-li batteries (Na, K, Mg, and Ca) *Chem. Mater.* 31 8613–28
- [16] Tinker H R, Howard C A, Zhou M and Xu Y 2023 Exploring anodes for calcium-ion batteries Mater. Adv. 4 2028-41
- [17] You C, Wu X, Yuan X, Chen Y, Liu L, Zhu Y, Fu L, Wu Y, Guo Y-G and van Ree T 2020 Advances in rechargeable Mg batteries J. Mater. Chem. A 8 25601–25
- [18] Aurbach D, Lu Z, Schechter A, Gofer Y, Gizbar H, Turgeman R, Cohen Y, Moshkovich M and Levi E 2000 Prototype systems for rechargeable magnesium batteries Nature 407 724–7
- [19] Li D, Yuan Y, Liu J, Fichtner M and Pan F 2020 A review on current anode materials for rechargeable Mg batteries (available at: https://publikationen.bibliothek.kit.edu/1000126647) (Accessed 22 September 2024)
- [20] Sun Q, Luo S, Huang R, Yan S and Lin X 2024 Recent progress of magnesium electrolytes for rechargeable magnesium batteries Coord. Chem. Rev. 515 215956
- [21] Aurbach D, Skaletsky R and Gofer Y 1991 The electrochemical behavior of calcium electrodes in a few organic electrolytes J. Electrochem. Soc. 138 3536–45
- [22] Wang D, Gao X, Chen Y, Jin L, Kuss C and Bruce P G 2018 Plating and stripping calcium in an organic electrolyte Nat. Mater. 17 16–20
- [23] Ponrouch A, Frontera C, Bardé F and Palacín M R 2016 Towards a calcium-based rechargeable battery Nat. Mater. 15 169–72
- [24] Forero-Saboya J, Davoisne C, Dedryvère R, Yousef I, Canepa P and Ponrouch A 2020 Understanding the nature of the passivation layer enabling reversible calcium plating Energy Environ. Sci. 13 3423–31
- [25] Li Z, Fuhr O, Fichtner M and Zhao-Karger Z 2019 Towards stable and efficient electrolytes for room-temperature rechargeable calcium batteries Energy Environ. Sci. 12 3496–501
- [26] Shyamsunder A, Blanc L E, Assoud A and Nazar L F 2019 Reversible calcium plating and stripping at room temperature using a borate salt ACS Energy Lett. 4 2271–6

- [27] Forero-Saboya J D, Marchante E, Araujo R B, Monti D, Johansson P and Ponrouch A 2019 Cation solvation and physicochemical properties of Ca Battery Electrolytes J. Phys. Chem. C 123 29524–32
- [28] Mandai T, Naya H and Masu H 2023 Comparative studies on [B(HFIP)₄]-Based electrolytes with mono- and divalent cations J. Phys. Chem. C 127 7987–97
- [29] Li S, Zhang J, Zhang S, Liu Q, Cheng H, Fan L, Zhang W, Wang X, Wu Q and Lu Y 2024 Cation replacement method enables high-performance electrolytes for multivalent metal batteries Nat. Energy 9 285–97
- [30] Pavčnik T, Forero-Saboya J D, Ponrouch A, Robba A, Dominko R and Bitenc J 2023 A novel calcium fluorinated alkoxyaluminate salt as a next step towards Ca metal anode rechargeable batteries *J. Mater. Chem. A* 11 14738–47
- [31] Ceppetelli A, Castilla-Martinez C, Rousselot E, Monconduit L, Demirci U B, Brutti S and Stievano L 2025 CaB₁₂H₁₂: a promising salt for aprotic electrolytes in calcium-based secondary batteries J. Energy Storage 108 115012
- [32] Bodin C et al 2023 Boron-based functional additives enable solid electrolyte interphase engineering in calcium metal battery Batteries Supercaps 6 e202200433
- [33] Forero-Saboya J, Bodin C and Ponrouch A 2021 A boron-based electrolyte additive for calcium electrodeposition Electrochem. Commun. 124 106936
- [34] Zhao Y, Wang A, Ren L, Liu X and Luo J 2022 Revealing the solid electrolyte interface on calcium metal anodes *J. Energy Chem.* 70 174–90
- [35] Song H, Li Y, Tian F and Wang C 2022 Electrolyte optimization and interphase regulation for significantly enhanced storage capability in Ca-metal batteries Adv. Funct. Mater. 32 2200004
- [36] Arulepp M, Permann L, Leis J, Perkson A, Rumma K, Jänes A and Lust E 2004 Influence of the solvent properties on the characteristics of a double layer capacitor J. Power Sources 133 320–8
- [37] Moumouzias G, Panopoulos D K and Ritzoulis G 1991 Excess properties of the binary liquid system propylene carbonate + acetonitrile J. Chem. Eng. Data 36 20–3
- [38] Winter M 2009 the solid electrolyte interphase—the most important and the least understood solid electrolyte in rechargeable li batteries *Z. Phys. Chem.* 223 1395–406
- [39] Hilbig P, Ibing L, Streipert B, Wagner R, Winter M and Cekic-Laskovic I 2018 Acetonitrile-based electrolytes for lithium-ion battery application Curr. Top. Electrochem. 20 1
- [40] Nilsson V, Younesi R, Brandell D, Edström K and Johansson P 2018 Critical evaluation of the stability of highly concentrated LiTFSI—Acetonitrile electrolytes vs. graphite, lithium metal and LiFePO₄ electrodes *J. Power Sources* 384 334—41
- [41] Hayashi M, Arai H, Ohtsuka H and Sakurai Y 2003 Electrochemical characteristics of calcium in organic electrolyte solutions and vanadium oxides as calcium hosts J. Power Sources 119 617–20
- [42] Matsuoka N, Kamine H, Natsume Y and Yoshino A 2021 Moderately concentrated acetonitrile-containing electrolytes with high ionic conductivity for durability-oriented lithium-ion batteries ChemElectroChem 8 3095–104
- [43] Li M, Liu Y, Yang X, Zhang Q, Cheng Y, Deng L, Zhou Q, Cheng T and Gu M D 2024 Acetonitrile-based local high-concentration electrolytes for advanced lithium metal batteries Adv. Mater. 2404271
- [44] Gagne R R, Koval C A and Lisensky G C 1980 Ferrocene as an internal standard for electrochemical measurements *Inorg. Chem.* 19 2854–5
- [45] Stöckel W and Schumacher R 1987 In situ microweighing at the junction metal/electrolyte Ber. Bunsenges. Phys. Chem. 91 345–9
- [46] Biria S, Pathreeker S, Genier F S, Chen F-H, Li H, Burdin C V and Hosein I D 2021 Gel polymer electrolytes based on cross-linked poly(ethylene glycol) diacrylate for calcium-ion conduction ACS Omega 6 17095–102
- [47] Lin H, Meng J, Guo W, Li R, Yi Y, Ma Y, Cheung C F, Aurbach D and Xu Z-L 2024 Deciphering the dynamic interfacial chemistry of calcium metal anodes *Energy Environ. Sci.* 17 6548–58
- [48] Lipson A L, Proffit D L, Pan B, Fister T T, Liao C, Burrell A K, Vaughey J T and Ingram B J 2015 Current collector corrosion in Ca-Ion batteries J. Electrochem. Soc. 162 A1574—8
- [49] Yang S et al 2025 Revisiting the interfacial chemistry of calcium metal anodes: the importance of inorganic-rich solid/electrolyte interfaces derived from an aggregation-dominated electrolyte Energy Environ. Sci. 18 1941–51
- [50] Sudha V and Sangaranarayanan M V 2002 Underpotential deposition of metals: structural and thermodynamic considerations J. Phys. Chem. B 106 2699–707
- [51] Biria S, Pathreeker S, Li H and Hosein I D 2019 Plating and stripping of calcium in an alkyl carbonate electrolyte at room temperature ACS Appl. Energy Mater. 2 7738–43
- [52] Melemed A M and Gallant B M 2020 Electrochemical signatures of interface-dominated behavior in the testing of calcium foil anodes I. Electrochem. Soc. 167 140543
- [53] Forero-Saboya J D, Lozinšek M and Ponrouch A 2020 Towards dry and contaminant free Ca(BF₄)₂-based electrolytes for Ca plating J. Power Sources Adv. 6 100032
- [54] Dereka B, Lewis N H C, Keim J H, Snyder S A and Tokmakoff A 2022 Characterization of acetonitrile isotopologues as vibrational probes of electrolytes J. Phys. Chem. B 126 278–91